中国激光

搅拌摩擦辅助激光直接沉积AlSi10Mg显微组织和强韧性研究

赵海生[1,2]，张峰[2]，杜成超[3*]，任旭东[3]，魏翔宇[2]，高俊杰[2]

[1]中国航发北京航空材料研究院，北京 100095；

[2]航发优材（镇江）增材制造有限公司，江苏 镇江 212132；

[3]江苏大学材料科学与工程学院，江苏 镇江 212013

摘要 采用搅拌摩擦辅助激光定向能量沉积方法制备了AlSi10Mg合金块体，采用后续冷轧处理进一步提高了AlSi10Mg合金的强度，系统讨论了AlSi10Mg合金在加工过程中的组织演化，分析了其强韧性的演变机理。研究结果表明：在激光沉积态AlSi10Mg合金中，Si原子的固溶强化效果非常显著，合金的硬度高达109 HV，受气孔缺陷影响，激光沉积AlSi10Mg合金的强度低于200 MPa。搅拌摩擦加工可以细化激光沉积AlSi10Mg合金的柱状α-Al相和共晶相，形成等轴的α-Al晶粒和Si颗粒，α-Al基体中的Si原子脱溶析出，其硬度降低至75 HV，强度接近200 MPa，延伸率最高达到40%。轧制后，AlSi10Mg合金中的位错密度大幅增加，当变形量增加到68%时，AlSi10Mg合金α-Al晶粒被剧烈细化，合金的硬度被提高至116 HV，其强度可超过400 MPa，合金中的局部硬化区域导致其塑性变形能力下降，延伸率逐渐降低至25%。

关键词 激光技术；搅拌摩擦辅助激光沉积；AlSi10Mg合金；固溶强化；位错强化；韧性

中图分类号 TG456.7 **文献标志码** A **DOI**：10.3788/CJL230976

1 引 言

基于激光定向能量沉积的激光增材制造具有柔性、高效、有热输入量小、热影响区小、熔覆层组织致密等优势，近年来备受关注[1-6]。相较于铺粉的激光选区熔化技术，该技术适用面广、增材制造效率高，广泛应用于航天航空、轨道交通、海工装备领域的零件修复[7-11]。

激光沉积高强铝合金是零件修复领域的难点[12-13]，以Al-Zn-Mg-Cu系列为代表的高强铝合金的合金元素含量高，合金在凝固过程中半固态区间较宽，甚至超过100 ℃，较宽的半固态区间极易在铝合金的α-Al晶粒之间留下“液膜”，在热应力的作用下，“液膜”开裂，形成裂纹[14-15]。此外较高的冷却速度也导致气孔难以溢出，最终在合金中留下气孔缺陷[16-17]。

AlSi10Mg合金作为一种铸造铝合金[18]，具有半固态区间较短、强度较高、密度低、耐蚀性好的特点[19-20]，非常适用于高强铝合金构件的增材制造和激光修复。然而在激光沉积时，工艺波动常导致构件中出现气孔等缺陷[21]，这类缺陷在构件服役过程中极易导致裂纹萌生，最终造成构件失效，因此，探索一种消除AlSi10Mg激光沉积构件中气孔的方法对于提升AlSi10Mg构件的力学性能和服役寿命具有重要意义。

搅拌摩擦加工（FSP）源于搅拌摩擦焊接，利用搅拌头对材料的热-机作用改善成分偏析、细化晶粒、消除缺陷，是一种改善铝合金显微组织的常用方法。大量的研究表明搅拌摩擦加工能够提升细晶强化的能力[22-24]。此外，搅拌摩擦加工还能够促进强化相弥散分布，提升沉淀强化的能力[25-27]。因此，将激光沉积和搅拌摩擦加工相结合制备高强韧AlSi10Mg合金构件，具有重要的科研价值和现实意义。

本文立足于搅拌摩擦加工辅助激光沉积AlSi10Mg合金的强韧化。首先对比了沉积态合金和搅拌摩擦加工态合金的显微组织和力学性能，揭示了固溶强化、细晶强化、沉淀强化对AlSi10Mg合金强韧性的影响规律。然后研究了冷轧对搅拌摩擦加工态AlSi10Mg合金显微组织和力学性能的影响，揭示了位错强化对AlSi10Mg合金强韧性的影响规律。最后系统揭示了AlSi10Mg合金中固溶强化、细晶强化、沉淀强化、位错强化的作用机理。

收稿日期：2023-06-30；**修回日期**：2023-08-21；**录用日期**：2023-10-11；**网络首发日期**：2023-10-25

基金项目：国家自然科学基金（52205369）、江苏省自然科学基金（BK20210756）、江苏省博士后基金（2021K035A）

通信作者：*dccmaterials@ujs.edu.cn

2 实验材料及方法

本文采用的气雾化 AlSi10Mg 合金粉末粒径为 53～150 μm。在激光沉积过程中，激光功率为 2700 W，沉积速度为 600 mm/min，送粉速度为 5.8 g/min，搭接量为 2.5 mm，送粉氩气流量为 5 L/min，保护氩气流量为 20 L/min，使得单层的厚度为 0.5 mm。沉积 8 层至 4 mm 后，对沉积态 AlSi10Mg 合金进行搅拌摩擦加工，搅拌头的搅拌针的高度为 4 mm，形状为四棱柱，棱柱端部直径为 6 mm，如图 1(a)所示。搅拌摩擦加工时，转速为 800 r/min，搅拌速度为 100 mm/min，搅拌摩擦加工道次之间的偏移量为 5 mm。在搅拌摩擦加工后的 AlSi10Mg 合金表面继续激光沉积 8 层 AlSi10Mg 合金，再采用搅拌摩擦加工，如图 1(b)所示。最终的 AlSi10Mg 合金如图 1(c)所示。

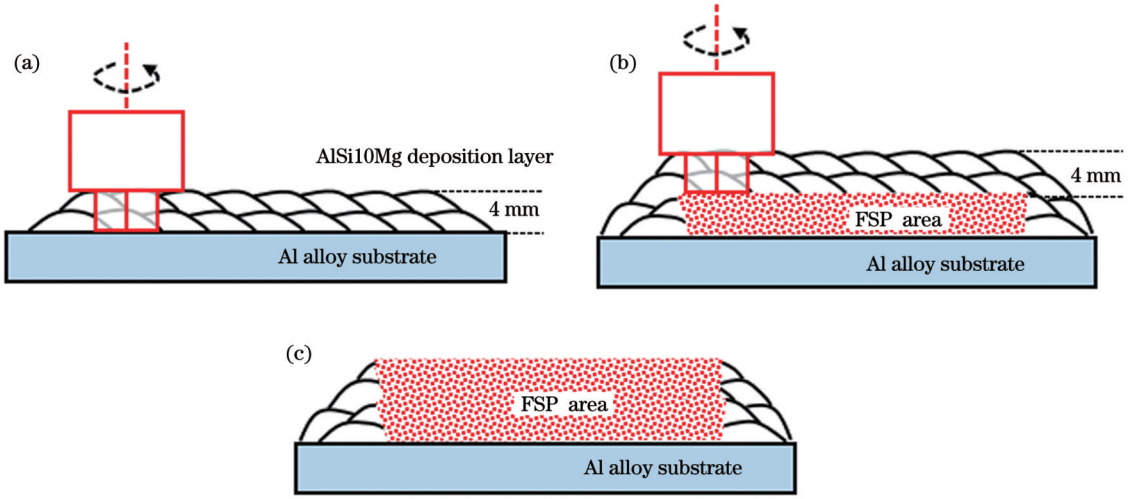

图 1 搅拌摩擦辅助激光沉积过程示意图。(a)搅拌摩擦加工 1-2 层沉积层，(b)搅拌摩擦加工 3-4 层沉积层，(c)搅拌摩擦加工后的 1-4 沉积层

Fig. 1 Schematics of FSP-assisted laser deposition. (a) Friction stir processing of 1st and 2nd deposition layers; (b) friction stir processing of 3rd and 4th deposition layers; (c) 1st, 2nd, 3rd, and 4th deposition layers after FSP

采用电火花线切割截取搅拌摩擦辅助激光沉积 AlSi10Mg 合金，对该合金进行后续的室温轧制处理，轧制变形量分别为 20%、46%、68%，从而得到 5 种 AlSi10Mg 合金，加工参数如表 1 所示。加工以上 5 种 AlSi10Mg 合金的拉伸试样，采用拉伸试验机测定 5 种 AlSi10Mg 合金的强度，拉断后根据试样上的标记点测量试样的延伸率。加工 5 种 AlSi10Mg 合金的金相试样，振动抛光后采用扫描电子显微镜(SEM)和背散电子衍射仪(EBSD)观察其显微组织。析出相尺寸的测量采用 Photoshop 软件，选取相互靠近的 20 个析出相，通过像素换算得到其面积，进而计算得到平均粒径。采用显微硬度计测定其显微硬度。制取 5 种 AlSi10Mg 合金的薄膜试样，电解双喷后，采用透射电子显微镜(TEM)观测其显微组织。拉伸试样的断口采用扫描电子显微镜进行观测。

表 1 AlSi10Mg 合金的加工参数

Table 1 Processing parameters of AlSi10Mg alloys

No.	Processing parameter
1	Laser deposition
2	Laser deposition+FSP
3	Laser deposition+FSP+rolling with 20% deformation
4	Laser deposition+FSP+rolling with 46% deformation
5	Laser deposition+FSP+rolling with 68% deformation

3 实验结果及讨论

3.1 激光沉积 AlSi10Mg 合金的显微组织

激光沉积 AlSi10Mg 合金的显微组织如图 2 所示。从图 2(a)可以发现，激光沉积 AlSi10Mg 合金中存在明显的气孔缺陷，显微组织的高倍图片如图 2(b)所示，该区域的元素面分布如图 2(c)～(e)所示。根据图 2(b)的组织形态和图 2(c)的 Si 元素分布，可将图 2(b)所示的相分为初生 α-Al 相和共晶相。凝固过程中 α-Al 相首先从液相中析出，当液相的温度达到共晶温度时，剩余液相迅速转变为共晶相，从 SEM 图片可以看出共晶相由 Si 颗粒和 α-Al 相共同构成。

激光沉积 AlSi10Mg 合金的 TEM 显微组织如图 3 所示。从图 3(a)可以发现，该区域存在较大的 Si 颗粒，该区域应为共晶相区域，其中 α-Al 相中存在较多 Mg_2Si 颗粒，尺寸约为 400 nm，部分呈长条状，部分呈颗粒状。进一步观察可以发现，凝固过程中存在一些位错，如图 3(b)所示，纳米级 Mg_2Si 颗粒与这些位错之间存在一定的交互作用。

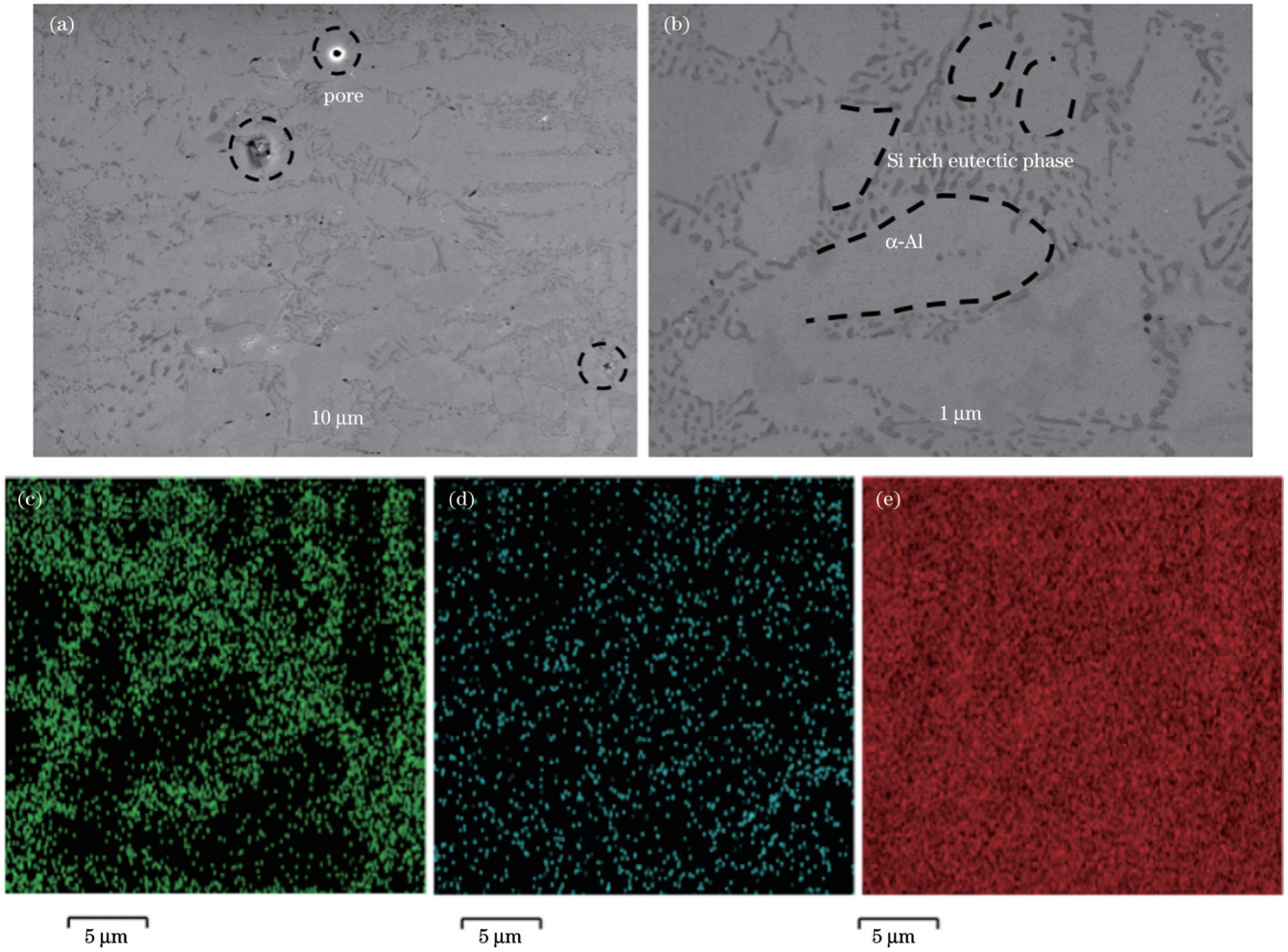

图 2　激光沉积 AlSi10Mg 合金的显微组织。(a)显微组织形貌;(b)图 2(a)的局部放大;(c) Si 元素面分布;(d) Mg 元素面分布;(e) Al 元素面分布

Fig. 2　Microstructure of laser deposited AlSi10Mg alloy. (a) Microstructure; (b) local magnification of Fig. 2(a); (c) Si mapping; (d) Mg mapping; (e) Al mapping

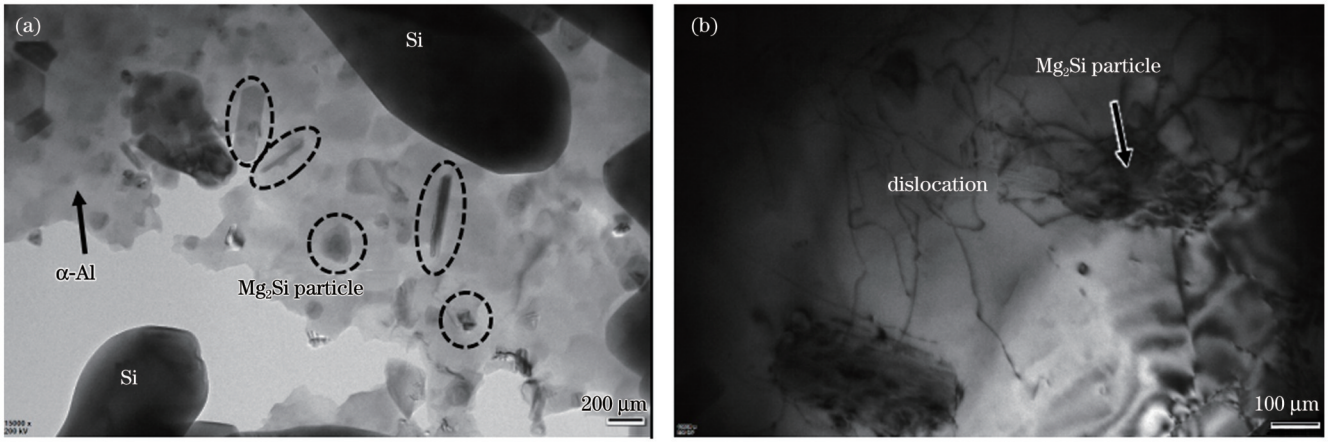

图 3　激光沉积 AlSi10Mg 合金的 TEM 组织特征。(a)α-Al、Si 相、Mg_2Si 颗粒分布;(b)位错与 Mg_2Si 颗粒的作用

Fig. 3　Microstructural characterization of AlSi10Mg alloy from TEM. (a) Distributions of α-Al, Si phase, and Mg_2Si particle; (b) interaction between dislocation and Mg_2Si particle

激光沉积 AlSi10Mg 合金的晶粒取向分布如图 4 所示。从图 4(a)、(b)可以发现,激光沉积 AlSi10Mg 合金中存在大量的气孔,初生 α-Al 相的晶粒形态往往呈现柱状特征。图 4(b)区域的极图如图 4(c)~(e)所示。从该区域的{100}极图可以发现,该区域存在较显著的择优取向,强度最大值为 3.97,择优取向的方向基本与柱状晶生长方向一致,如图 4(b)、(c)所示。

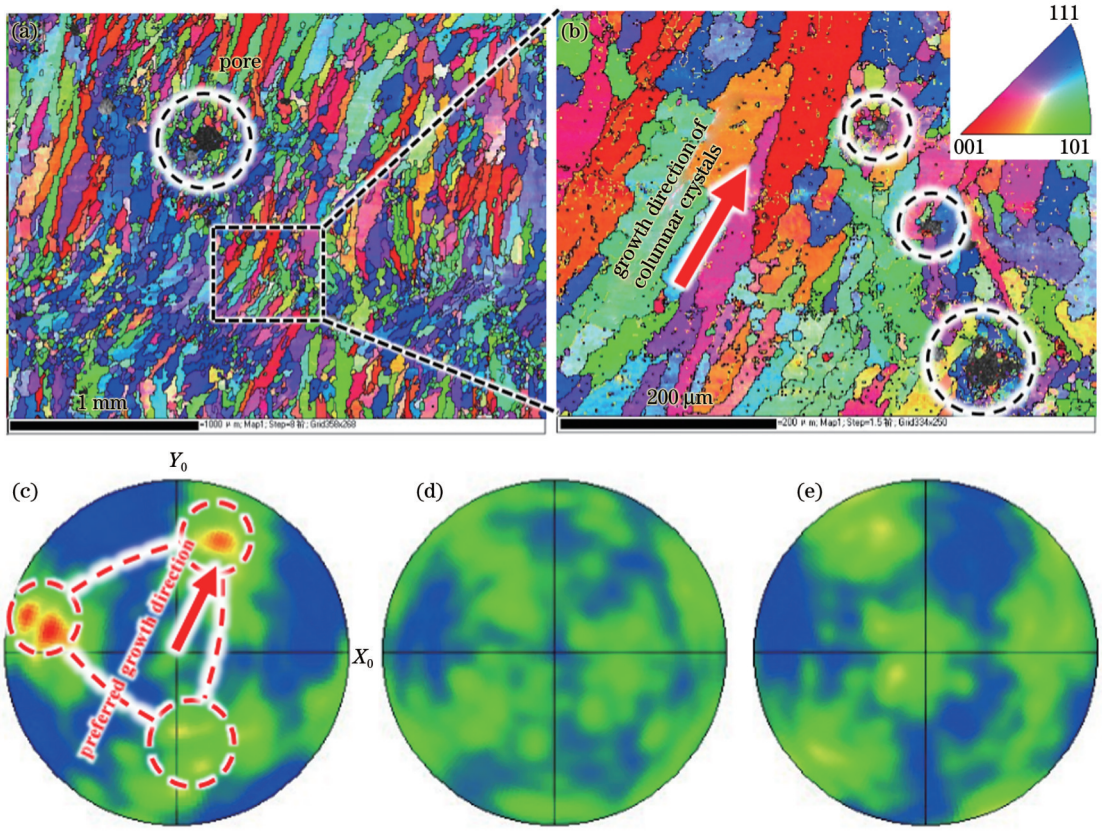

图 4　激光沉积 AlSi10Mg 合金的 EBSD 组织特征。(a)(b)晶粒取向分布;(c)｛100｝极图;(d)｛110｝极图;(e)｛111｝极图

Fig. 4　Microstructural characterization of AlSi10Mg alloy from EBSD. (a)(b) Grain orientation distributions; (c) {100} pole figure; (d) {110} pole figure; (e) {111} pole figure

3.2　搅拌摩擦加工对激光沉积 AlSi10Mg 合金的显微组织的影响

搅拌摩擦加工后激光沉积 AlSi10Mg 合金的显微组织如图 5 所示,可以发现,搅拌摩擦加工后的 AlSi10Mg 合金不再呈现初生 α-Al 和共晶相的显微形貌,AlSi10Mg 合金中的 Si 颗粒呈弥散分布,颗粒尺寸为(0.8±0.4) μm。

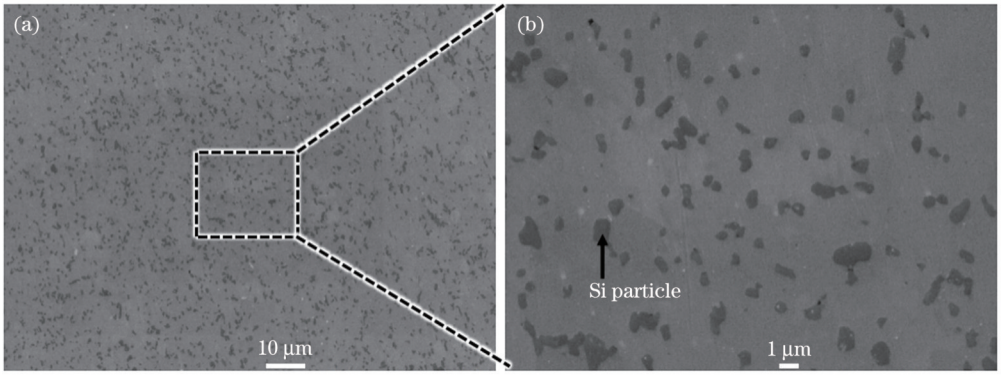

图 5　FSP 辅助激光沉积 AlSi10Mg 合金的显微组织。(a)宏观形貌;(b)微观形貌

Fig. 5　Microstructures of FSP-assisted laser deposited AlSi10Mg alloy. (a) Macro-morphology; (b) micro-morphology

搅拌摩擦加工后激光沉积 AlSi10Mg 合金的 TEM 显微组织如图 6 所示,可以发现,此时的显微组织由 α-Al 晶粒和 Si 颗粒构成,其中 α-Al 晶粒的尺寸约为 4.5 μm,Si 颗粒的尺寸约为 1.5 μm。进一步观察 α-Al 晶粒内部可以发现较多弥散分布的 Mg_2Si 相,基本呈颗粒状,尺寸约为 150 nm,如图 6(b)所示。Mg_2Si 颗粒阻碍 α-Al 晶粒内部的位错运动,如图 6(c)、(d)所示。

搅拌摩擦加工 AlSi10Mg 合金的衍射带衬度和晶粒取向分布分别如图 7(a)、(b)所示,可以发现 α-Al 晶粒在搅拌作用下被轻微拉长,长轴约为短轴的 2.7 倍。图 7(b)区域的极图如图 7(c)～(e)所示,可以发现该区域的织构较强,织构强度达到了 10.46。

在搅拌摩擦加工过程中,AlSi10Mg 合金在搅拌头和轴肩摩擦热的共同作用下不断塑化,在摩擦力作用下,塑化金属被不断剪切,最终其晶粒在剪切方向上被拉长,同时也形成了一定的织构,如图 7(c)所示。

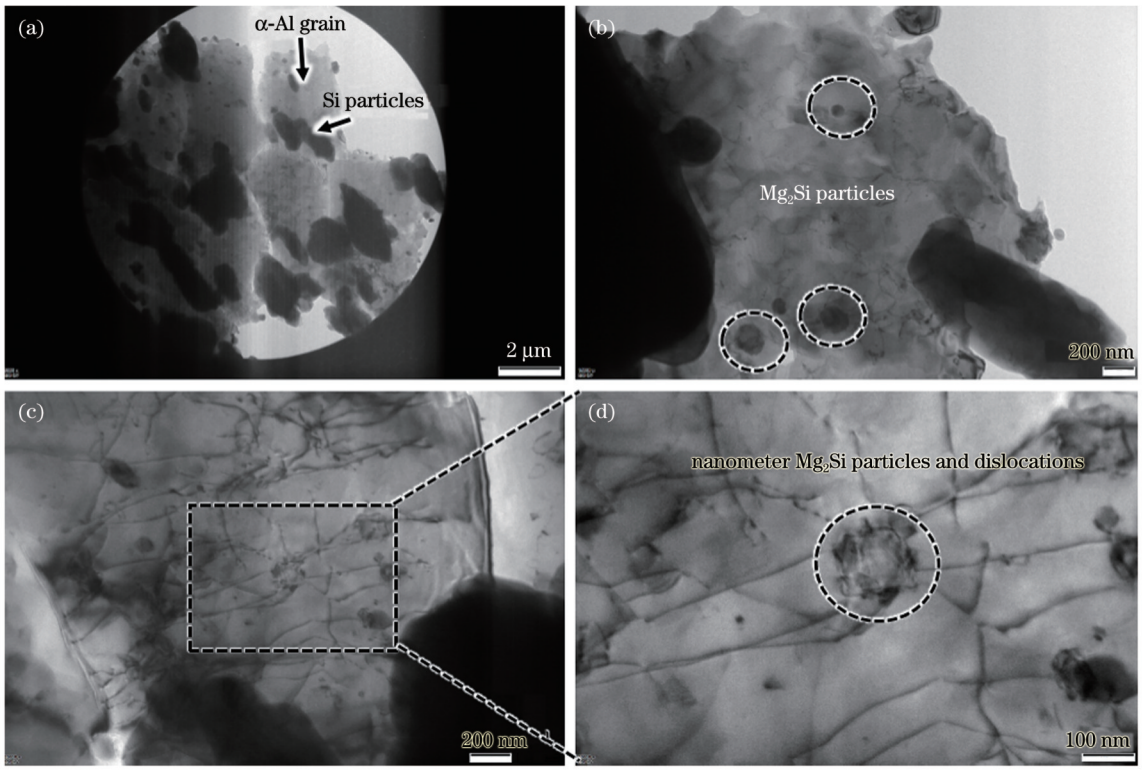

图 6　FSP 辅助激光沉积 AlSi10Mg 合金的 TEM 组织特征。(a) α-Al 和 Si 颗粒分布；(b) Mg_2Si 颗粒分布；(c)(d)位错与 Mg_2Si 颗粒的作用

Fig. 6　Microstructural characterization of FSP-assisted laser deposited AlSi10Mg from TEM. (a) Distribution of α-Al and Si particle; (b) Mg_2Si particle distribution; (c)(d) interaction between dislocation and Mg_2Si particle

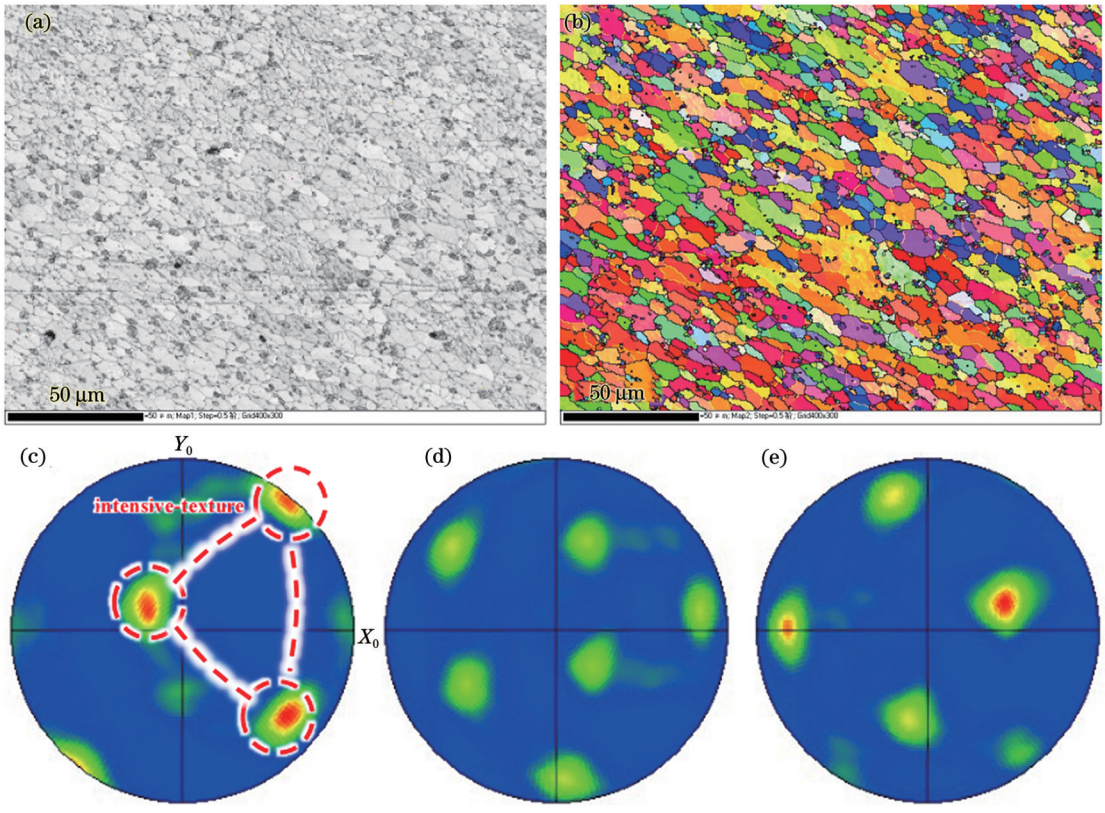

图 7　FSP 辅助激光沉积 AlSi10Mg 合金的 EBSD 组织特征。(a)衍射带衬度图；(b)晶粒取向分布图；(c){100}极图；(d){110}极图；(e){111}极图

Fig. 7　Microstructural characterization of FSP-assisted laser deposited AlSi10Mg alloy from EBSD. (a) Diffraction band contrast image; (b) grain orientation distribution; (c) {100} pole figure; (d) {110} pole figure; (e) {111} pole figure

3.3 冷轧对搅拌摩擦加工激光沉积 AlSi10Mg 合金的显微组织的影响

FSP 辅助冷轧激光沉积 AlSi10Mg 合金的 TEM 显微组织如图 8 所示，在冷轧过程中 AlSi10Mg 没有相变，其显微组织的演变主要为位错密度的增加和晶粒的细化。变形量为 20% 和 46% 的 AlSi10Mg 合金的显微组织如图 8(a)、(b)所示，可以发现其冷轧后期 α-Al 晶粒内部的位错大量增多。变形量为 68% 的 AlSi10Mg 合金的显微组织如图 8(c)所示，可以看出，α-Al 晶粒“破碎”，形成亚晶粒，亚晶粒尺寸约为 400 nm。此外，可以发现冷轧工艺对 Si 颗粒没有显著的影响。

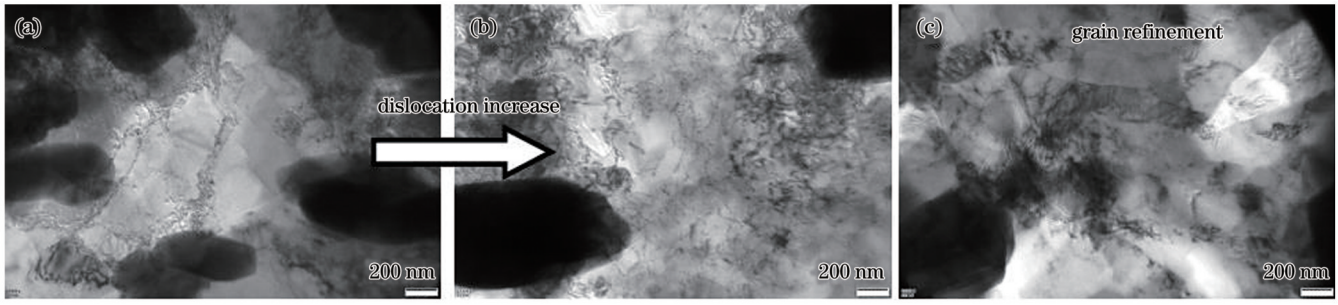

图 8　冷轧后 FSP 辅助激光沉积 AlSi10Mg 合金的 TEM 组织特征。(a)变形量 20%；(b)变形量 46%；(c)变形量 68%

Fig. 8　Microstructural characterization of FSP-assisted laser deposited AlSi10Mg alloy from TEM after cool rolling. (a) 20% deformation; (b) 46% deformation; (c) 68% deformation

3.4 FSP 辅助冷轧对激光沉积 AlSi10Mg 合金的力学性的影响

5 种状态 AlSi10Mg 合金的硬度如表 2 所示，可以发现沉积态 AlSi10Mg 合金的硬度约为 109 HV，搅拌摩擦加工后，AlSi10Mg 合金的硬度降低到 75 HV。从前文的研究可以发现：沉积态和搅拌态 AlSi10Mg 合金的位错密度均较低，因此其位错强化的差异并不大；搅拌摩擦加工后 α-Al 基体内的 Mg_2Si 强化相较沉积态更细小，Mg_2Si 的沉淀强化效果应优于沉积态；搅拌摩擦加工后，AlSi10Mg 合金的晶粒更加细小，其细晶强化效果也应优于沉积态。因此，搅拌摩擦加工后，AlSi10Mg 合金的细晶强化和沉淀强化的效果优于沉积态，理论上其硬度也应该较沉积态高，但搅拌摩擦态的硬度却显著低于沉积态。

表 2　AlSi10Mg 合金的硬度

Table 2　Hardnesses of AlSi10Mg alloys

No.	1	2	3	4	5
Hardness /HV	109±4	75±7	89±5	101±3	116±6

AlSi10Mg 合金是一种极度依赖固溶强化的铝合金[28-29]，高温下 Si 元素在 α-Al 基体中的固溶度较大，当温度迅速降低时，Si 元素难以从 α-Al 基体中脱溶，大量 Si 原子在 α-Al 基体中起到了固溶强化作用，因此，激光沉积态 AlSi10Mg 合金的硬度高达 109 HV。搅拌摩擦加工的温度约为 450 ℃，在该温度下，Si 原子逐渐从 α-Al 基体中脱溶析出，形成 Si 颗粒，因此，Si 原子的固溶强化效果逐渐下降。此外，尽管搅拌摩擦加工后合金的晶粒细化，细晶强化效果有所提升，但这仍不能弥补固溶强化的损失，因此合金的硬度降低至 75 HV。

从表 2 中轧制态的 AlSi10Mg 的硬度可以发现，轧制工艺能显著提升 AlSi10Mg 合金的硬度，当轧制变形量达到 68% 时，其硬度达到了 116 HV，超过了沉积态的 109 HV。从前文的研究可以发现，轧制能够逐渐提升搅拌摩擦加工后激光沉积 AlSi10Mg 合金的位错密度，当轧制变形量进一步提升时，合金的晶粒逐步细化。因此，轧制工艺提升了 AlSi10Mg 合金中位错强化和细晶强化的效果，最终将搅拌摩擦加工后激光沉积 AlSi10Mg 合金的硬度提升到 116 HV。

5 种状态 AlSi10Mg 合金的抗拉强度和延伸率的分布如图 9 所示，其中 WD 为搅拌摩擦加工方向，TD 为垂直于搅拌摩擦加工方向的方向。可以发现，沉积态 AlSi10Mg 合金的强度较低，抗拉强度低于 200 MPa，延伸率低于 20%，其强塑性关系与文献[30-33]中研究的 AlSi10Mg 合金的下限接近。搅拌摩擦加工

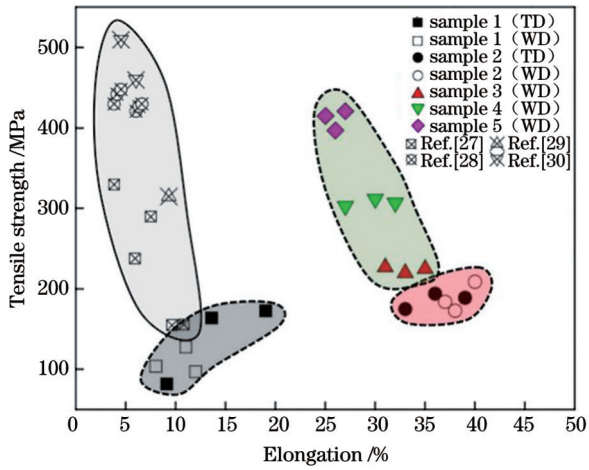

图 9　AlSi10Mg 合金的抗拉强度与延伸率分布图

Fig. 9　Distributions of tensile strength and elongation of AlSi10Mg alloys

后，AlSi10Mg 合金的强度接近 200 MPa，延伸率为 33%～40%，可见搅拌摩擦加工能够同时提升激光沉积 AlSi10Mg 合金的强度和塑性。

激光沉积态和搅拌摩擦加工态 AlSi10Mg 合金的拉伸断口如图 10 所示，可以观察到激光沉积态 AlSi10Mg 合金的拉伸断口中存在大量气孔缺陷和韧窝，搅拌摩擦加工态 AlSi10Mg 合金的断口表面未观察到气孔等缺陷，断口上有大量的韧窝特征，可以断定两种状态 AlSi10Mg 合金的断裂模式均为塑性断裂模式。

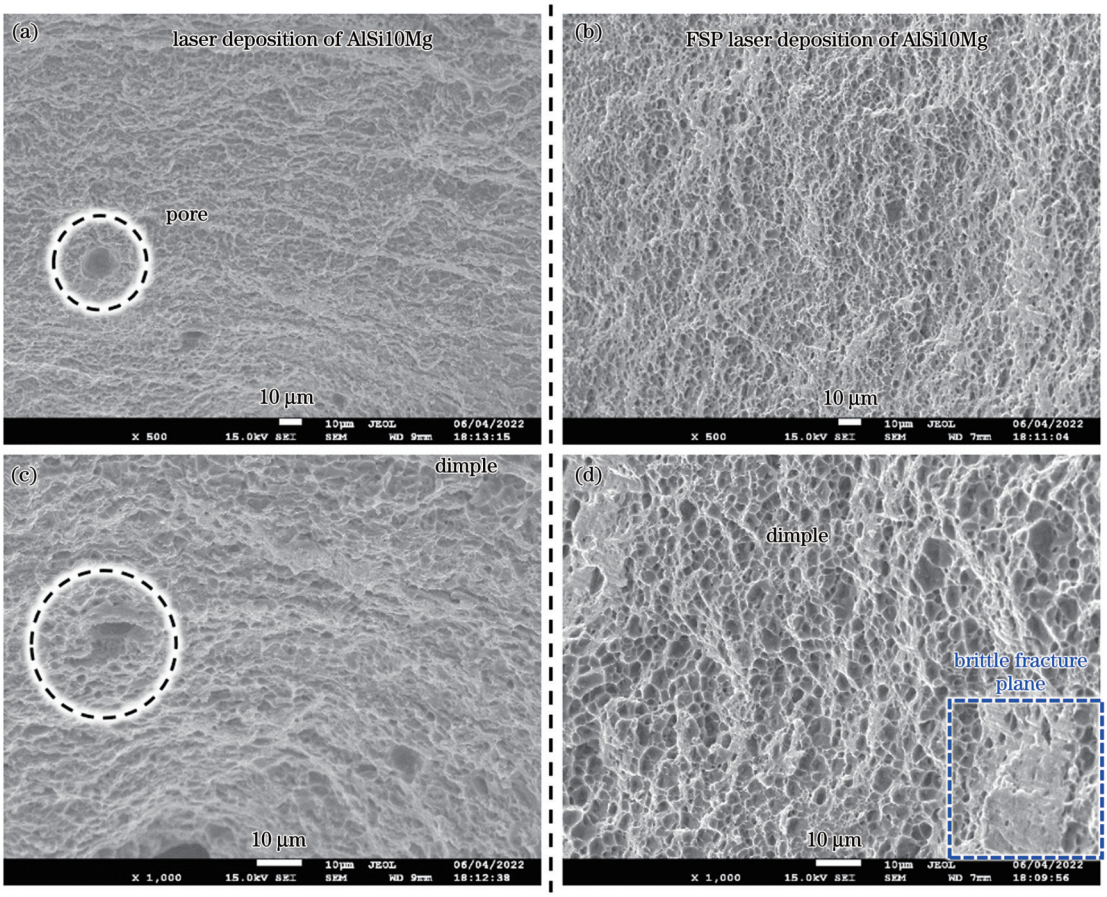

图 10 激光沉积 AlSi10Mg 合金和 FSP 辅助激光沉积 AlSi10Mg 合金的拉伸断口。(a)激光沉积 AlSi10Mg 合金；(b) FSP 激光沉积 AlSi10Mg 合金；(c)图 10(a)的局部放大；(d)图 10(b)的局部放大

Fig. 10 Tensile fractures of laser deposited and FSP-assisted laser deposited AlSi10Mg alloys. (a) Laser deposited AlSi10Mg alloy; (b) FSP-assisted laser deposited AlSi10Mg alloy; (c) local magnification of Fig. 10(a); (d) local magnification of Fig. 10(b)

硬度的研究结果表明，沉积态 AlSi10Mg 合金的固溶强化效果优于搅拌摩擦加工态，因此其强度应该高于搅拌摩擦加工态，但激光沉积 AlSi10Mg 合金中存在气孔缺陷，在拉伸过程中这些缺陷造成试样内部的应力集中，导致试样内部微区的早期开裂，因此，激光沉积态 AlSi10Mg 合金的强度和延伸率均不能达到较高的水平。而搅拌摩擦加工后，较大的轴肩压力和搅拌作用消除了合金中的气孔缺陷，拉伸时内部应力集中程度较轻，因此其延伸率大幅提高。

轧制后的 AlSi10Mg 合金的强度随延伸率的变化如图 9 所示，可以发现轧制后 AlSi10Mg 合金的强度随着轧制变形量的增加而逐渐增加，当轧制变形量达到 68% 时，其强度达到了约 400 MPa。然而，AlSi10Mg 合金的延伸率却表现出与强度相反的变化趋势，延伸率随着轧制变形量的增加而逐渐降低，当轧制变形量达到 68% 时，AlSi10Mg 合金的延伸率降低到约 26%。

三种轧制后的 AlSi10Mg 合金的拉伸断口如图 11 所示，可以发现，AlSi10Mg 合金的断口中存在两种区域，一种是塑性断裂的韧窝特征，另一种是脆性断裂区域。同时可以发现，随着轧制变形量的增加，脆性断裂区域的比例逐渐增加。

轧制工艺在 AlSi10Mg 合金中引入了大量的位错，位错在微区缠结，形成了局部硬化区，在拉伸过程中，局部硬化区的变形能力较差，不能发生显著的塑性变形，因此，表现出局部的脆性断裂特征。此外，轧制变形量的逐渐增加导致局部硬化区域的占比增大，因此 AlSi10Mg 合金的塑性变形能力逐渐变差，断口中脆性断裂区域的占比逐渐增加，延伸率逐渐下降。

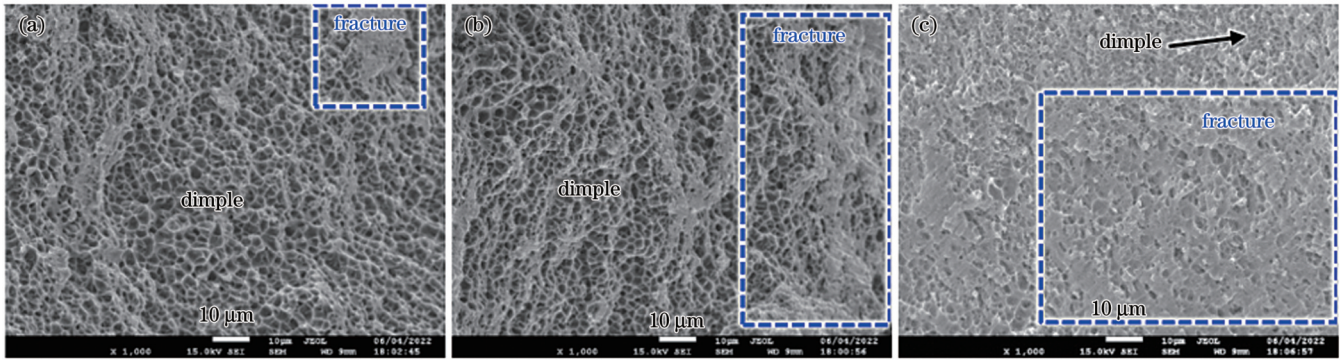

图 11 轧制后 FSP 辅助激光沉积 AlSi10Mg 合金的拉伸断口。(a)变形量 20%;(b)变形量 46%;(c)变形量 68%

Fig. 11 Tensile fractures of FSP-assisted laser deposited AlSi10Mg alloys after rolling. (a) 20% deformation; (b) 46% deformation; (c) 68% deformation

4 结 论

研究了激光沉积、搅拌摩擦加工、轧制对 AlSi10Mg 合金的组织和性能的影响,系统地讨论了 AlSi10Mg 合金在加工过程中的组织演化,分析了其强韧性的演变机理,得到的结论如下:

1) 搅拌摩擦加工后,激光沉积 AlSi10Mg 合金的柱状 α-Al 相和共晶相组织被搅拌碎化,形成了等轴的 α-Al 晶粒和 Si 颗粒,且 Mg_2Si 沉淀相被显著细化。轧制后,AlSi10Mg 合金中的位错密度大幅增加,变形量增加到 68% 时,AlSi10Mg 合金的 α-Al 晶粒被进一步细化。

2) 激光沉积 AlSi10Mg 合金中的 Si 具有较强的固溶强化效果,这使得激光沉积态 AlSi10Mg 合金的硬度高达约 109 HV。搅拌摩擦加工后,尽管合金中的细晶强化和沉淀强化效果更好,但这仍不能弥补固溶强化的损失,AlSi10Mg 合金的硬度仅有约 75 HV。轧制后,合金中的位错强化效果显著加强,此外加大轧制量还带来了部分细晶强化效果,因此,AlSi10Mg 合金的硬度最多提升到 116 HV,超过了激光沉积 AlSi10Mg 合金的显微硬度。

3) 尽管激光沉积 AlSi10Mg 合金中的固溶强化效果显著,但在拉伸过程中,合金中的凝固缺陷导致早期裂纹的形成,合金的强度低于 200 MPa,延伸率低于 20%。搅拌摩擦加工后,AlSi10Mg 合金的韧性得到提升,强度接近 200 MPa,延伸率为 33%~40%。轧制后,AlSi10Mg 合金的位错强化效果逐渐增加,其强度持续上升,最高达到约 400 MPa,合金中的局部硬化区域导致其塑性变形能力下降,延伸率逐渐降低至约 26%。

参 考 文 献

[1] 尹续臣, 刘建荣, 王清江, 等. 激光直接沉积 TC17/TC11 双合金的组织及性能[J]. 稀有金属材料与工程, 2020, 49(3): 1024-1030.
Yin X C, Liu J R, Wang Q J, et al. Microstructure and tensile properties of TC17/TC11 dual alloy fabricated with laser melting deposition method[J]. Rare Metal Materials and Engineering, 2020, 49(3): 1024-1030.

[2] 苏传出, 陈希章, Sergey Konovalov, 等. 激光直接沉积 CoCrFeNiMn 高熵合金:气孔-组织结构-拉伸性能之间的关系[J]. 材料工程, 2022, 50(3): 43-49.
Su C C, Chen X Z, Konovalov S, et al. Direct laser deposited CoCrFeNiMn high-entropy alloys: relationship between pores-microstructure-tensile properties[J]. Journal of Materials Engineering, 2022, 50(3): 43-49.

[3] Wang S Y, Cui L, Liu G, et al. Effects of laser powers on the microstructure and wear resistance of molybdenum coatings prepared by supersonic laser deposition[J]. Surface and Coatings Technology, 2023, 453: 129142.

[4] 吴影, 刘艳, 陈文静, 等. 超高速激光熔覆技术研究现状及其发展方向[J]. 电焊机, 2020, 50(3): 1-10, 140.
Wu Y, Liu Y, Chen W J, et al. Research status and development direction of ultra-high speed laser cladding technology[J]. Electric Welding Machine, 2020, 50(3): 1-10, 140.

[5] 赵建光, 侯娟, 熊孝经. 基于激光直接沉积技术的增减材复合制造核用 304L 不锈钢接头性能研究[J]. 电焊机, 2020, 50(7): 39-45, 148.
Zhao J G, Hou J, Xiong X J. Study on the properties of 304L stainless steel joint for nuclear use by composite manufacturing of additive and subtractive materials based on laser direct deposition technology[J]. Electric Welding Machine, 2020, 50(7): 39-45, 148.

[6] 金宸宇, 葛鸿浩, 张亚周, 等. 激光熔覆 316L 粉末多层堆积过程中熔覆层 Cr 元素分布机制研究[J]. 中国激光, 2023, 50(12): 1202205.
Jin C Y, Ge H H, Zhang Y Z, et al. Distribution mechanism of Cr element in laser cladding layer during 316L powder multilayer stacking[J]. Chinese Journal of Lasers, 2023, 50(12): 1202205.

[7] 梁旭峰, 蔡振华, 刘琦, 等. 压气机叶片激光熔化沉积修复的机器人路径自动规划和试验研究[J/OL]. 航空制造技术: 1-8[2023-01-02]. http: //kns. cnki. net/kcms/detail/11.4387. v. 20221027. 0946.006.html.
Liang X F, Cai Z H, Liu Q, et al. Laser melting deposition repair for compressor blades: robotic path automatic planning and experimental analysis [J/OL]. Aeron. Manu. Technol: 1-8[2023-01-02]. http: //kns. cnki. net/kcms/detail/11.4387. v. 20221027. 0946.006.html.

[8] Li Z H, Chai L J, Tang Y, et al. 316L stainless steel repaired layers by weld surfacing and laser cladding on a 27SiMn steel: a comparative study of microstructures, corrosion, hardness and wear performances[J]. Journal of Materials Research and Technology, 2023, 23: 2043-2053.

[9] Zhang B, He B, Wang H M. Microstructural investigation and mechanical performance of laser cladding repaired bainite steel with AerMet100 steel[J]. Surface and Coatings Technology, 2022,

440: 128498.

[10] 刘建琴, 郭晓, 张鑫, 等. 隧道掘进机滚刀涂层的激光熔覆修复实验与仿真研究[J]. 天津大学学报(自然科学与工程技术版), 2023, 56(1): 103-110.
Liu J Q, Guo X, Zhang X, et al. Experimental and simulation study on laser cladding repair of hob coating of tunnel boring machine[J]. Journal of Tianjin University (Science and Technology), 2023, 56(1): 103-110.

[11] 李柏泓, 郭绍庆, 周标, 等. 激光直接沉积钛合金热力耦合模型的建立与验证[J]. 激光与光电子学进展, 2022, 59(11): 1114007.
Li B H, Guo S Q, Zhou B, et al. Establishment and verification of thermo-mechanical coupled model for laser direct deposition of titanium alloy[J]. Laser & Optoelectronics Progress, 2022, 59(11): 1114007.

[12] 折洁, 祝弘滨, 邱莹, 等. 铝镁钪锆铝合金粉末激光增材修复7B05铝合金显微组织及力学性能研究[J]. 现代城市轨道交通, 2022(5): 87-93.
Zhe J, Zhu H B, Qiu Y, et al. Study on the microstructure and mechanical properties of 7B05 aluminum alloy repaired via laser additive with Al-Mg-Sc-Zr aluminum alloy powder[J]. Modern Urban Transit, 2022(5): 87-93.

[13] 王小艳, 陈静, 林鑫, 等. AlSi12粉激光成形修复7050铝合金组织[J]. 中国激光, 2009, 36(6): 1585-1590.
Wang X Y, Chen J, Lin X, et al. Microstructures of laser forming repair 7050 aluminum alloy with AlSi12 powder[J]. Chinese Journal of Lasers, 2009, 36(6): 1585-1590.

[14] 刘新亮. 激光选区熔化YSZ/7075铝合金成形工艺及性能研究[D]. 广州: 广东工业大学, 2021.
Liu X L. Study on forming process and properties of YSZ/7075 aluminum alloy by laser selective melting[D]. Guangzhou: Guangdong University of Technology, 2021.

[15] 李跃. 合金元素对半连铸7×××铝合金微观组织和热裂敏感性的影响研究[D]. 北京: 北京科技大学, 2019.
Li Y. Effect of alloying elements on microstructure and hot cracking sensitivity of semi-continuous casting 7××× aluminum alloy[D]. Beijing: University of Science and Technology Beijing, 2019.

[16] 夏丰滨. 汽车用7000系铝合金激光焊接接头组织与性能研究[D]. 北京: 北京有色金属研究总院, 2013.
Xia F B. Study on microstructure and properties of laser welded joint of 7000 series aluminum alloy for automobile[D]. Beijing: General Research Institute for Nonferrous Metals, 2013.

[17] 徐荣, 王文军, 祝弘滨, 等. 激光定向能量沉积Al-Mg-Sc-Zr修复5083-H112铝合金的组织和性能[J]. 材料工程, 2024, 52(2): 40-49.
Xu R, Wang W J, Zhu H B, et al. Microstructure and properties of repaired 5083-H112 aluminum alloy by laser direct energy deposited Al-Mg-Sc-Zr[J]. Journal of Materials Engineering, 2024, 52(2): 40-49.

[18] 张继祥, 刘嘉源, 李欢, 等. AlSi10Mg合金选区激光熔化大层厚成型及热处理工艺参数研究[J]. 重庆交通大学学报(自然科学版), 2022, 41(8): 149-156.
Zhang J X, Liu J Y, Li H, et al. Study on forming and heat treatment parameters of $AlSi_{10}Mg$ alloy with large thickness by selective laser melting[J]. Journal of Chongqing Jiaotong University (Natural Science), 2022, 41(8): 149-156.

[19] 丁莹, 杨海欧, 白静, 等. 激光立体成形AlSi10Mg合金的微观组织及力学性能[J]. 中国表面工程, 2018, 31(4): 46-54.
Ding Y, Yang H O, Bai J, et al. Microstructure and mechanical property of AlSi10Mg alloy prepared by laser solid forming[J]. China Surface Engineering, 2018, 31(4): 46-54.

[20] 闫泰起, 陈冰清, 唐鹏钧, 等. 铺粉层厚对选区激光熔化成形AlSi10Mg合金质量及效率的影响[J]. 中国激光, 2021, 48(10): 1002106.
Yan T Q, Chen B Q, Tang P J, et al. Effect of layer thickness on forming quality and efficiency of AlSi10Mg alloy fabricated by selective laser melting[J]. Chinese Journal of Lasers, 2021, 48(10): 1002106.

[21] Tridello A, Fiocchi J, Biffi C A, et al. Size-effects affecting the fatigue response up to 10^9 cycles (VHCF) of SLM AlSi10Mg specimens produced in horizontal and vertical directions[J]. International Journal of Fatigue, 2022, 160: 106825.

[22] 彭滔. 7075铝合金搅拌摩擦加工及急停的组织性能研究[D]. 重庆: 重庆大学, 2013.
Peng T. Study on microstructure and properties of friction stir processing and emergency stop of 7075 aluminum alloy[D]. Chongqing: Chongqing University, 2013.

[23] Jiang J Y, Jiang F, Zhang M H, et al. Microstructure evolution and tensile property of deformed Al-Mg-Sc alloy: comparison of ECAP and FSP[J]. Journal of Materials Research and Technology, 2023, 22: 2612-2626.

[24] 叶奔, 丁强, 秦未, 等. 多道次搅拌摩擦加工制备的5083铝合金细晶材料超塑性研究[J]. 浙江理工大学学报(自然科学版), 2017, 37(4): 502-505.
Ye B, Ding Q, Qin W, et al. Superplastic study of AA5083 aluminum alloy processed by multi-pass friction stir technology[J]. Journal of Zhejiang Sci-Tech University (Natural Sciences Edition), 2017, 37(4): 502-505.

[25] Narimani M, Lotfi B, Sadeghian Z. Investigating the microstructure and mechanical properties of Al-TiB_2 composite fabricated by Friction Stir Processing (FSP)[J]. Materials Science and Engineering: A, 2016, 673: 436-442.

[26] 乔元鹏. 原位自生Al_3Zr颗粒增强铝基复合材料的搅拌摩擦加工及其组织与性能研究[D]. 镇江: 江苏科技大学, 2022.
Qiao Y P. Friction stir processing of *in-situ* Al_3Zr particle reinforced aluminum matrix composites and its microstructure and properties[D]. Zhenjiang: Jiangsu University of Science and Technology, 2022.

[27] 孙焕焕, 祝李洋, 武小娟, 等. 铸态7075铝合金搅拌摩擦加工微观组织和性能研究[J]. 沈阳理工大学学报, 2019, 38(3): 7-15.
Sun H H, Zhu L Y, Wu X J, et al. Study of microstructure and properties of cast 7075 aluminum alloy by friction stir processing [J]. Journal of Shenyang Ligong University, 2019, 38(3): 7-15.

[28] 杨天野, 崔丽, 贺定勇, 等. 选区激光熔化AlSi10Mg-Er-Zr合金微观组织及力学性能强化[J]. 金属学报, 2022, 58(9): 1108-1117.
Yang T Y, Cui L, He D Y, et al. Enhancement of microstructure and mechanical property of AlSi10Mg-Er-Zr alloys fabricated by selective laser melting[J]. Acta Metallurgica Sinica, 2022, 58(9): 1108-1117.

[29] 奥妮, 何子昂, 吴圣川, 等. 激光增材制造AlSi10Mg合金的力学性能研究进展[J]. 焊接学报, 2022, 43(9): 1-19, 113.
Ao N, He Z A, Wu S C, et al. Recent progress on the mechanical properties of laser additive manufacturing AlSi10Mg alloy[J]. Transactions of the China Welding Institution, 2022, 43(9): 1-19, 113.

[30] Bosio F, Phutela C, Ghisi N, et al. Tuning the microstructure and mechanical properties of AlSi10Mg alloy via *in-situ* heat-treatments in laser powder bed fusion[J]. Materials Science and Engineering: A, 2023, 879: 145268.

[31] Zhu S M, Katti I, Qiu D, et al. Microstructural analysis of the influences of platform preheating and post-build heat treatment on mechanical properties of laser powder bed fusion manufactured AlSi10Mg alloy[J]. Materials Science and Engineering: A, 2023, 882: 145486.

[32] Eom Y S, Park J M, Choi J W, et al. Fine-tuning of mechanical properties of additively manufactured AlSi10Mg alloys by controlling the microstructural heterogeneity[J]. Journal of Alloys and Compounds, 2023, 956: 170348.

[33] Chen S Q, Tan Q Y, Gao W Q, et al. Effect of heat treatment on the anisotropy in mechanical properties of selective laser melted AlSi10Mg[J]. Materials Science and Engineering: A, 2022, 858: 144130.

Microstructure and Strength-Toughness of FSP-Assisted Laser Deposited AlSi10Mg Alloy

Zhao Haisheng[1,2], Zhang Feng[2], Du Chengchao[3*], Ren Xudong[3], Wei Xiangyu[2], Gao Junjie[2]

[1]*AECC Beijing Institute of Aeronautical Materials, Beijing* 100095, *China*;

[2]*HFYC (Zhenjiang) Additive Manufacturing Co., Ltd., Zhenjiang* 212132, *Jiangsu, China*;

[3]*School of Materials Science and Engineering, Jiangsu University, Zhenjiang* 212013, *Jiangsu, China*

Abstract

Objective In recent years, laser additive manufacturing based on direct laser deposition has attracted widespread attention because of its flexibility and efficiency. This technology has a wide range of applications and high additive manufacturing efficiency. It is widely used in the aerospace, rail transit, and ship component maintenance equipment fields. However, high-strength aluminum alloys such as those in the Al-Zn-Mg-Cu series have a high content of alloying elements. During the solidification process, the semi-solid range of the alloy may exceed 100 ℃, which can easily leave gaps between aluminum grains. The α-Al layer of "liquid film" generates cracks under the action of thermal stress, making laser deposition repair difficult. AlSi10Mg alloy, as a cast aluminum alloy, has the characteristics of a short semi-solid range and high strength, and is suitable for additive manufacturing and the laser repair of high-strength aluminum alloy components. However, during the laser deposition process, process fluctuations often cause defects such as pores to appear in the components, leading to cracks and ultimately component failure during use. Therefore, exploring a method to eliminate pores in components produced using AlSi10Mg laser deposition is of great significance for improving the mechanical properties and service life of AlSi10Mg components.

Methods Atomized AlSi10Mg alloy powder with a particle size ranging from 53 μm to 150 μm is adopted. During the laser deposition process, the laser power is 2700 W, deposition speed is 600 mm/min, powder feed rate is 5.8 g/min, overlap amount is 2.5 mm, argon flow rate is 5 L/min, and protective argon amount is 20 L/min, resulting in a single-layer thickness of 0.5 mm. After depositing eight layers to achieve a thickness of 4 mm, stir friction treatment is performed on the deposited AlSi10Mg alloy. The height of the mixing needle of the mixing head is 4 mm, with a four-prism shape and diameter of 6 mm at the end of the prism. During the stirring friction treatment process, the rotational speed is 800 r/min, stirring speed is 100 mm/min, and variation in the stirring friction treatment passes is 5 mm. Subsequently, the laser deposition of eight-layer AlSi10Mmg alloy is continued on the surface of the AlSi10Mg alloy after the stir friction machining, and then stir friction machining is used.

Wire cutting is used to cut the AlSi10Mg alloy into five samples, and stir friction-assisted laser deposition is conducted, followed by room-temperature rolling treatment. Rolling deformation values of 20%, 46%, and 68% are achieved on three of the samples. The five tensile specimens of the AlSi10Mg alloy are treated as mentioned above, and their strength and elongation values are measured using a tensile testing machine. After vibration polishing, the five metallographic samples are observed using a scanning electron microscope and backscattered electron diffractometer, and their microhardness values are measured. A thin film sample of the AlSi10Mg alloy is prepared and its microstructure is observed using a transmission electron microscope after electrolytic double spraying. The fracture of the tensile specimen is observed using the scanning electron microscope.

Results and Discussions The hardness values of the AlSi10Mg alloy in the five different states are listed in Table 1. It can be observed that the hardness of the deposited AlSi10Mg alloy is approximately 109 HV. Because at high temperatures, the solid solubility of the Si element in the α-Al matrix is relatively high, and when the temperature rapidly drops, it is difficult for the Si element to recover from α-Al matrix, and a large number of Si atoms on α-Al matrix play a role in solid solution strengthening. The Al matrix plays a role in solid solution strengthening. After stir friction processing, the solid solution strengthening effect is significantly weakened, and the hardness of the AlSi10Mg alloy decreases to 75 HV. Based on the hardness values of the rolled AlSi10Mg specimens listed in Table 2, it can be observed that the rolling process improves the effects of dislocation strengthening and fine grain strengthening in the AlSi10Mg alloy, ultimately increasing the hardness of the laser-deposited AlSi10Mg alloy after stir friction processing to 116 HV. As shown in Fig. 9, after stir friction processing, the strength of the AlSi10Mg alloy is close to 200 MPa, and the elongation distribution is 33%–40%. It can be seen that stir friction processing can simultaneously improve the strength and plasticity of the laser-deposited AlSi10Mg alloy. Figure 10 shows that there are a large number of dimples in the tensile fracture surface of the AlSi10Mg alloy in the laser deposition state and stir friction processing state, indicating that the fracture mode of both AlSi10Mg alloy specimens is the plastic fracture mode. The research on hardness shows that the strength and elongation of the laser deposited AlSi10Mg alloy cannot reach high levels. However, after stir friction processing, the larger shoulder pressure and stirring effect eliminate the porosity defects in the alloy, reduce the stress concentration, and thus significantly increase its elongation.

Conclusions After friction stir processing, the columnar α-Al and eutectic phases in the laser deposited AlSi10Mg become equiaxed α-Al grains and Si particles, while the Mg_2Si precipitate phase is significantly refined. After rolling, when the deformation of the AlSi10Mg alloy increases to 68%, dislocation strengthening further refines the grains.

After rolling, the dislocation strengthening effect in the alloy is significantly enhanced. In addition, increasing the rolling amount also brings about a fine grain strengthening effect. Therefore, the hardness of the AlSi10Mg alloy can be increased to 116 HV at most, exceeding the microhardness of the laser deposited AlSi10Mg alloy.

Although the solid solution strengthening effect in the laser deposited AlSi10Mg alloy is remarkable, the solidification defects in the alloy lead to the formation of early cracks during the tensile process, which results in an alloy strength of less than 200 MPa and an elongation of less than 20%. After friction stir processing, the strength and toughness of the AlSi10Mg alloy are simultaneously improved, with a strength close to 200 MPa and an elongation of 33%–40%. After rolling, the dislocation strengthening effect of the AlSi10Mg alloy gradually increases, and its strength continues to rise, reaching a maximum of approximately 400 MPa. The localized hardening area in the alloy leads to a decrease in its plastic deformation ability, and the elongation gradually decreases to 25%.

Key words laser technique; friction stir processing-assisted laser deposition; AlSi10Mg alloy; solid solution strengthening; dislocation strengthening; toughness